Dynamical mechanisms controlling formation and avalanche of a stagnant slab

T. Nakakuki[1]*, M. Tagawa[1]** and Y. Iwase[2]

1. Department of Earth and Planetary Systems Science,
Hiroshima University
2. Department of Marine and Earth Science,
National Defense Academy

* Corresponding author (nakakuki@hiroshima-u.ac.jp)
** Now at TERRAPUB, Tokyo

Submitted to "Physics of the Earth and Planetary Interiors" on 13 Oct., 2009.
Revised on 28 Jan., 2010.
Accepted on 5 Feb., 2010.

Abstract

We performed a numerical study to understand the dynamical mechanism controlling the formation and avalanche of a stagnant slab using two-dimensional dynamical models of the integrated plate-mantle system with freely movable subducting and overriding plates. We examined slab rheology as a mechanism for producing various styles of stagnating or penetrating slabs that interact with the 410-km and 660-km phase transitions. The simulated results with the systematically changed rheological parameters are interpreted using a simple stability analysis that includes the forces acting on the stagnant slab. Slab plasticity that memorizes the shape produced by past deformation generates slab stagnation at various depths around the 660-km phase transition. The slab stagnates even beneath the 660-km phase boundary, with a gentle Clapeyron slope. Feedbacks between trench backward migration and slab deformation promote each other during the slab stagnation stage. Slab viscosity also determines the final state of the subducted slab, that is, it continues stagnation or initiates penetration. A low-viscosity slab can finally penetrate into the lower mantle because the growth time of the Rayleigh-Taylor instability is shorter. After the avalanche, the direction of the trench migration changes depending on the lower mantle slab viscosity.

1. Introduction

Seismic tomography images variable structures of subducted slabs (van der Hilst et al., 1991; Fukao et al., 1992; review by Fukao et al, 2001). Some subducted slabs stagnate horizontally not only above the 660-km discontinuity but also in the mantle transition zone or beneath the 660-km discontinuity, and others penetrate into the deep lower mantle. Seismological observations show cessation of deep seismicity at about 700 km depth (e.g., Frohlich, 1989). The focal mechanisms always indicate down-dip compression in the deep slabs above the 660-km discontinuity (e.g., Isacks and Molnar, 1971). These observations also imply that convective flow to the lower mantle is impeded at least partly.

The 660-km discontinuity is inferred as a phase transition from ringwoodite (Rw) to decomposed perovskite (Pv) and magnesiowüstite (Mw) with a negative Clapeyron slope (Akaogi et al., 1989; Katsura and Ito, 1989) that behaves as a barrier against penetration of a cold slab (e.g., Schubert et al., 2001; review by Tackley, 1995). Christensen and Yuen (1984) performed numerical simulation of the subducting slab interacting with phase and/or chemical boundaries using models with temperature- and stress-dependent viscosity. Nakakuki et al. (1994) and Davies (1995) emphasized the important effects of the viscosity on flow penetration with comparing plume and slab interaction with the phase boundary. They posed the important question of what mechanism enables the highly viscous slab to stagnate with a Clapeyron slope as gentle as -3 MPa K^{-1}.

Slab stagnation above the 660-km discontinuity is often accompanied by trench retreat, that is, backward migration of the subducted slab (van der Hilst and Seno, 1993). The seismic structure of the transition zone slab determined by waveform modeling (Tajima and Grand, 1998; Shito and Shibutani, 2001) indicated a relationship between trench motion inferred from reconstruction of the Philippine Sea plate (Seno and Maruyama, 1984) and a stagnant slab in the Izu-Bonin-Mariana subduction zone. Based on these tectonic considerations, Christensen (1996) showed that trench retreat imposed to the surface of his models strongly influences the styles of transition zone slab. On the other hand, Karato et al. (2001) pointed out the relationship between the age of the subducted lithosphere and the slab structure, and they concluded that the slab viscosity reduction due to the grain-size reduction that was accompanied by the phase transition (Rubie, 1984; Karato, 1989; Riedel and Karato, 1997) is a more important mechanism controlling the slab structure. Čížková et al. (2002) produced stagnant slabs in a semi-dynamic numerical model with yielding and grain-size reduction to reduce the bending strength of the slab. Their models indicate that trench retreat controls the slab structure more than rheological strength reduction. Torii and Yoshioka (2007) found that a viscosity jump generates a stagnant slab under conditions that include trench retreat less than 2 cm yr^{-1}, even when the Clapeyron slope of the 660-km discontinuity is 0 MPa K^{-1}. A recent review by Billen (2008) summarized effects of the slab and surrounding mantle viscosity and trench migration on the structure and the fate of subducted slabs. Fukao et al. (2009) compared various types of numerically simulated slabs with seismic tomography images. Although the dependence of the slab structure on rheological and tectonic parameters has been revealed, we do not have certain dynamical explanations for the simulated slab structures. Questions still remain of how trench retreat and phase boundary buoyancy mechanically control the behavior of the subducted lithosphere in the transition zone.

We also do not yet well understand dynamical mechanisms that generate trench retreat. The rollback of a gravitationally unstable slab (e.g., Molnar and Atwater, 1978; Sdrolias and Müller, 2006) is still considered to be a candidate for the main driving force of back-arc basin formation, because active back-arc opening accompanies a fast retreating slab (Heuret and Lallemand, 2005). Kincaid and Olson (1987) showed that trench retreat is induced by slab stagnation at the chemical boundary. Tagawa et al. (2007a) showed that backward slab motion is promoted when the phase transition impedes penetration into the lower mantle using a two-dimensional (2-D) numerical simulation of an integrated plate-mantle system. Zhong and Gurnis (1997) found forward slab motion during slab penetration in their 2-D global-scale convection model.

In this study, we concentrate our efforts on revealing how slab rheology in the transition zone controls the formation and avalanche of a stagnant slab. We construct 2-D dynamical models of the subduction system that interacts with the mantle phase transitions at 410-km and 660-km depths. In our model, plate motion and plate-boundary migration are generated dynamically without velocity conditions imposed on the plate as our previous studies (Tagawa et al., 2007b; Nakakuki et al., 2008). We introduce the viscosity reduction in the transition-zone and/or the lower-mantle slab because of the grain-size reduction that accompanies the phase transitions at 410-km (Rubie, 1984; Karato, 1989; Riedel and Karato, 1997; Shimojuku et al., 2004; Yamazaki et al., 2005) and 660-km (Ito and Sato, 1991; Karato et al, 1995; Kubo et al., 2000) depths. The importance of the slab plasticity is highlighted in the mechanism that determines the structure and the fate of the subducted plate. The results obtained will be examined based on a simple stability analysis of the stagnant slab. We also examine the mutual interactions between slab deformation and trench migration during the process of stagnant slab formation and its avalanche.

2. Model settings and basic equations

2.1 Model configuration

We trace the evolution of the developing slab interaction with the mantle transition zone under a freely movable and deformable overriding plate. A schematic view of the model configuration is shown in Fig. 1. The model is constructed based on the long-time integrated model in Nakakuki et al. (2008). Major changes from the previous model include: (1) the 410-km and 660-km phase transitions, (2) enlargement of the model size (10000 km $\times$ 2000 km), (3) the 6-km thick layer with history-dependent yielding (Tagawa et al., 2007b), and (4) viscosity and yield-stress reduction due to hydration in the wedge mantle area (see Section 2.3 for details). Several assumptions are made to produce the plate-like motion of the surface as mentioned in Nakakuki et al. (2008). The physical parameters are described in Table I.

We use an extended Boussinesq fluid model (Christensen and Yuen, 1985) in a 2-D rectangular box to minimize numerical difficulties from handling a complex rheology. Neither external forces nor velocities are imposed on the model boundaries in order to generate dynamic plate boundary migration. The internal buoyancy forces drive the lithosphere motion and underlying mantle flow. Free slip (tangential stress free) conditions are assigned to all the boundaries for the mechanical boundary condition. In the previous study, on the contrary, an imposed velocity boundary at the surface is employed because the total buoyancy of 3-D slabs controls the subducting plate motion (King and Ita, 1995; Christensen, 1996; Torii and Yoshioka; 2007). We assume that internal heating is equal to 0 because its heating effect is negligible for the short elapsed time (< 100 Myr) of our simulation. The temperature of the lowest 500-km-thick layer is fixed to that of the initial conditions (Segments 8 and 9, Fig. 1). Constant temperature is applied to the top boundary, and thermal insulation is on the bottom and both side boundaries.

The transition zone is modeled with two phase transitions of olivine series minerals: olivine to wadsleyite at the 410-km depth, and ringwoodite to perovskite and magnesiowüstite at the 660-km depth. In this study, the Clapeyron slope for the 410-km phase transition is set to be +3 MPa K^{-1} or +2 MPa K^{-1}, and that for the 660-km is -3 MPa K^{-1} or -2 MPa K^{-1}. These values are more consistent with those inferred from the depression of the 660-km discontinuity obtained by seismological study (e.g., Flanagan and Shearer, 1998) than those from recent high pressure experiments (Katsura et al., 2003; Fei et al., 2004). The density contrasts at phase boundaries are provided according to the PREM model (Dziewonski and Anderson, 1981). For the olivine composition model, the density contrasts are assumed to be 100% of the PREM density contrast (7.8 and 8.3% for the 410- and 660-km phase transitions, respectively) and for the pyrolite composition model (Irifune, 1993), it is 60% of the PREM density contrast.

2.2 Lithosphere settings and initial conditions

We consider initiating subduction of the oceanic lithosphere at the continental margin. The models consist of two lithospheres — “oceanic” and “continental.” The oceanic lithosphere is a surface layer with the same composition as that of the underlying mantle and a high viscosity due to its low temperature. The oceanic lithosphere has a layer with history-dependent yielding (Segment 2, Fig. 1) acting as a weak fault zone at the oceanic-continental plate boundary (Segment 3, Fig. 1). This simulates lubrication due to a wet oceanic crust. This layer does not have a density difference from the underlying mantle. The continental lithosphere includes an intrinsically buoyant layer simulating a continental crust 34 km thick (Segment 5, Fig. 1) and a low-temperature mantle lithosphere beneath the crust.

Because we examine the effects of the overriding plate motion, we introduce a condition in which the overriding plate is disconnected from the right-side boundary. The low viscosity zone is introduced to the top-right corner (Segment 6, Fig. 1). The viscosity of this zone is fixed at 10^{22} Pa·s, which is close to the effective viscosity of the orogenic zone (Gordon, 2000). The continental crust is placed between 6000 and 9000 km for the x-direction to avoid the low viscosity zone. The lateral density contrast ($d\rho/dx$) is set at 0 in the lower viscosity zone and the underlying area (Segment 10, Fig. 1) to avoid gravitational instability of the cold thermal boundary layer in this zone.

The oceanic lithosphere temperature in the initial conditions is determined according to the half-space cooling model with 0 to 100 Ma. The continental lithosphere temperature is set to the value of the oldest (100 Ma) oceanic lithosphere. The temperature in the underlying mantle is set to be adiabatic with a potential temperature of 1280 °C (Fig. 2). Temperature jumps due to latent heat at the phase boundaries are included in the initial temperature. To initiate subduction, we introduce a preexisting weak zone with the history-dependent yielding into the oceanic-continental plate boundary, according to

Tagawa et al. (2007b).

2.3 Rheology model

We use a viscous fluid model to approximate long-term mantle deformations. The viscosity depends on the temperature, pressure (depth), grain size, yield stress, and yielding history (Honda et al., 2000; Tagawa et al., 2007b; Nakakuki., et al., 2008). The effective viscosity (η) is given by an Arrhenius-type law including grain-size dependence when the stress is lower than the yield strength. According to Karato and Wu (1993), dislocation creep is dominant in the deformation mechanism in the shallow part of the upper mantle (asthenosphere) because the activation volume is larger than that for diffusion creep. We assume that the non-Newtonian rheology parameterized by reducing temperature and pressure dependence as an approximation (Christensen, 1984) governs the effective viscosity in the layer shallower than 300 km as follows:

$$\eta = \min\left[A d_r^{\ m} \exp\left[\frac{2}{n+1} \cdot \frac{E^* + pV^*}{R\left(T + T_0\right)} \right], \eta_L \right], \qquad (1)$$

where E^* is activation energy, p is hydrostatic pressure, V^* is activation volume, R is the gas constant, T is temperature, m (= 2) is a body-diffusion exponent of the grain size, and n (= 3) is the stress exponent. η_L is the viscosity limit to reduce the effective viscosity of the lithosphere at low temperature (Tagawa et al., 2007b). This value is varied to examine the effects of slab viscosity in the transition zone and/or the lower mantle on the slab structure. The viscosity-depth profile in the initial conditions is shown in Fig. 2. The pre-exponential factor A is fixed as it is equal to the reference viscosity $\eta_{ref} = 5\times10^{20}$ Pa·s at the depth of 410 km in the initial conditions. This is a mean value for the upper mantle obtained by the postglacial rebound study (Milne et al., 1999; Okuno and Nakada, 2001). The activation volume V^* is assumed to decrease linearly with depth as

$$V^* = V_0 + \left(V_L - V_0\right) z / h. \qquad (2)$$

The activation energy E^* and the activation volume at the surface V_0 are provided by values for a wet olivine according to Karato and Wu (1993). The activation volume at the bottom of V_L is determined as the mean value of the viscosities in the layer from a depth of 660 to 1500 km and coincides with the observed lower mantle viscosity (10^{22} Pa·s) derived by the postglacial rebound study (Milne et al., 1999; Okuno and Nakada, 2001).

The relative grain size d_r introduces the viscosity-grain size dependence. When the viscosity does not depend on the grain size, d_r is fixed at 1. When the grain-size dependence is considered, d_r is described as a linearized Arrhenius law (Čížková et al, 2002)

$$d_r = d_f \quad \text{at} \quad T < T_f, \tag{3}$$

$$d_r = \exp\left[\ln\left(\frac{1}{d_f}\right)\frac{T - T_c}{T_c - T_f}\right] \quad \text{at} \quad T_f \le T \le T_c, \tag{4}$$

and

$$d_r = 1 \quad \text{at} \quad T > T_c \ , \tag{5}$$

where is d_f the minimum relative grain size at temperatures lower than the minimum grain size temperature T_f.

We introduce yield stress with history dependence to generate the plate-like behavior of the surface layer as described in Tagawa et al. (2007b) and Nakakuki et al. (2008). When the stress reaches the yield strength, the effective viscosity is derived by

$$\eta = Y / 2\dot{\varepsilon}_{II} \quad \text{at} \quad \sigma_{II} = Y, \tag{6}$$

where Y is the yield stress, and σ_{II} and $\dot{\varepsilon}_{II}$ are the second invariants of stress and strain rate tensors. The value of Y depends on the segment. Except for the oceanic crust, the yield stress is expressed depending on the depth as

$$Y = \min\left[Y_0 + c_Y \rho_S g z, Y_m\right], \tag{7}$$

where Y_0 is the cohesive strength, c_Y is the friction coefficient of a brittle layer (Byerlee, 1978), ρ_S is the density at the surface, Y_m is the maximum yield strength concerned with brittle-ductile transition of the lithosphere (Kohlstedt, et al., 1995).

On the other hand, the yield stress in the oceanic crust depends on the past yielding history. In the intact material before its first yielding, the yield stress takes a value identical to that of the other segment. Once this segment fractures, its yield strength drops to a smaller value until it heals. The values of Y_0 and c_Y are changed to Y_F and c_F. In the initial conditions, a preexisting weak zone with the same strength as that of the fractured segment is assumed to initiate subduction at the "oceanic-continental" plate boundary. The strength of the spreading centre at the top-right corner is also set to be that of the fractured segment because of weakening by melting.

Because we seek to understand the feedback interactions between the slab deformation during the slab interaction with the mantle transition zone and the overriding plate deformation in the subduction zone, weakening of the wedge mantle and the overriding plate due to the slab dehydration is incorporated into the models (Peacock, 1991; Iwamori, 1998). We assume that the hydrous area is placed in the region above the slab in depths of 0 to 240 km (Segment 4, Fig. 1). This area is migrated and its shape is changed as the slab upper surface traced by the subducted oceanic crust segment (Segment 3, Fig. 1) moves. The activation energy E^* is reduced by 28.8 kJ $mol^{-1}K^{-1}$ for viscosity reduction. This value corresponds to about 150 K reduction of the melting temperature. The yield stress is also reduced in the hydrated region. At the tip of the overriding plate (continental crust) above the slab with a depth of 0 to 34 km, the material is assumed to be less hydrated so that the yield stress is set at a higher value than that of the lithosphere above the slab with a depth of 34 to 240 km.

2.4 Basic equations and numerical methods

The basic equations governing the models to be presented are the equations of continuity, motion, state, energy and mass transport. The equation of state determines density that is related to the temperature (T) in degrees Celsius, the composition function indicates compositional difference between the continental crust and the mantle (Γ_C), and the phase function expresses phase changes at the 410- and 660-km depths (Γ_{410} and Γ_{660}) by the equation of state

$$\rho = \rho_0 \left(1 - \alpha T\right) + \Delta\rho_C \left(1 - \Gamma_C\right) + \Delta\rho_{410}\Gamma_{410} + \Delta\rho_{660}\Gamma_{660}, \tag{8}$$

where ρ_C is the density difference between the continental crust and the mantle, ρ_{410} and ρ_{660} are the density difference at the 410-km and 660-km phase boundaries, respectively. According to Christensen and Yuen (1985), the phase functions are defined as

$$\Gamma_p = \frac{1}{2}\left[1 + \tanh\left(\frac{\pi_p}{d_p}\right)\right], \tag{9}$$

where d_p is the half thickness for the completion of the phase transition. The excess depth π_p is calculated from

$$\pi_p = z - z_p + \gamma_p \left(T - T_p\right), \tag{10}$$

where z_p is the phase transition depth at the phase transition temperature T_p, and γ_p is the Clapeyron slope of the phase transition. The subscript p is the index replaced by 410 or 660 for the 410- or 660-km phase transition, respectively.

The motion of the continental crust (Γ_C), the oceanic crust (the layer with history-dependent yielding, Γ_O), and the fractured segment (Γ_F) are governed by the equation of mass transport

$$\frac{\partial \Gamma_L}{\partial t} + \boldsymbol{u} \cdot \nabla \Gamma_L = 0, \tag{11}$$

where L is the index for the layers and is replaced by C, O, or F. The continental crust is represented by the position where $\Gamma_C = 1$. The oceanic crust in which the yield stress has history dependence is also expressed by the location where $\Gamma_O = 1$. We determine Γ_F which memorizes the history of yielding as follows: Before the first yielding, Γ_F is set to be 0. When the first yielding (the star, Fig. 1) occurs in the oceanic crust layer ($\Gamma_O = 1$: Segment 2, Fig. 1), $\Gamma_F = 1$ is imposed (Segment 3, Fig. 1). We also assume that the failure recovers at the 240-km depth, where Γ_F is reset to be 0. This simulates the effects of dehydration of the oceanic crust. This segment is used as an indicator of the slab surface to track the bottom and the side boundary of the hydrous area in the wedge mantle. In the initial condition, a segment with Γ_F of 1 is placed at the oceanic-continental plate boundary.

We employ a finite volume method developed by Tagawa et al. (2007b) to solve the equations. In this scheme, dual-layer grid space is adopted to discretize the equations. For the equation of energy and mass transport, the grid is uniform with 2×2 km spacing. For the equation of motion, the grid is non-uniform. The spacing of the control volumes (CVs) varies from region to region. The control volumes with the finest spacing (2×2 km) are placed in regions with intense viscosity variations such as divergent or convergent plate boundaries, or the transition zone under the subduction zone. The numbers of CVs for the x- and z-directions are 5000×1000 for the uniform grid, and 1678×308 for the non-uniform grid. A direct method (a modified Cholesky method) is applied to solve a band matrix generated by the discretized equation of motion. A cubic-interpolated pseudo-particle (CIP) method (Takewaki et al., 1985) is adopted for the equation of mass transport. The CIP method is established as a valid method to solve problems with sharp interfaces in computational fluid dynamics.

3. Results

3.1 The effects of slab rheology

We first concentrate our efforts on revealing how the slab viscosity controls the formation and avalanche of the stagnant slab. We therefore treat the rheological properties of transition zone slab as varying parameters, as shown in Table II. Various slab structures with varying slab rheologies near the final stage of the slab evolution are summarized in Fig. 3.

When the slab in the transition zone and the lower mantle has a high viscosity (10^{25} Pa·s) with pyrolite composition when γ= -2 (Case 1) and -3 MPa K^{-1} (Case 2: Fig. 3 (a)), the slab penetrates into the lower mantle even though the trench retreat occurs at about 4 cm yr^{-1}. The slab finally forms a horizontally lying shape at about 1000 km deep because the pressure-dependent viscosity increases viscous resistance. Because the stiff slab acts as a stress guide, the plate motion becomes as slow as 3 cm yr^{-1}. In the case when the material is composed of 100% olivine with a Clapeyron slope of -2 (Case 3: Fig 3(b)) and -3 MPa K^{-1} (Case 4), the slab penetration into the lower mantle is impeded so that a stagnant slab forms because the positive buoyancy of the 660-km phase transition is larger than when the material is composed of pyrolite. In these cases, the buoyancy of the phase transition has a substantial role in producing the stagnant slab, causing the slab to stagnate above the 660-km discontinuity. This type is hereafter called “phase-buoyancy” slab stagnation. This type of stagnation is shown as S(PB) in Table II.

When the truncation of the lower mantle slab viscosity is introduced, a stagnant slab is produced even in the case of the pyrolite models with the γ of -2 (Case 5) and -3 MPa K^{-1} (Case 6). The viscosity in the lower mantle slab is the identical to that in the ambient mantle. Snapshots of these cases are shown in Figs. 3 (c) and 3 (d), respectively. In Case 5, the slab temporarily stagnates at the 660-km phase transition and finally falls into the lower mantle. The positive buoyancy of the 660-km phase transition bends the subducted slab upward, although it cannot completely impede the slab penetration. Because of its plasticity, the slab memorizes the shape formed by this bending. The horizontally extended slab moves along the curled shape of the slab so that a horizontal slab structure is formed. While the horizontally extended slab cannot descend immediately, the tip of the slab climbs up into the upper mantle. Additionally, the horizontal slab broadens the phase boundary depression and thus increases the positive buoyancy. Because the shape-memory effect of the slab stiffness has an important role in generating the stagnant slab, this type of the stagnation is hereafter called “shape-memory” slab stagnation. It is indicated as S(SM) in Table II.

The evolution of Case 6 is shown in Fig. 4. In this case, the buoyancy of the 660-km phase transition is strong enough to temporarily generate slab stagnation above the phase transition, namely, “phase-buoyancy” stagnation occurs (Fig 4 (b)). The slab however continues to deform at the corner between the descending part and the stagnant part of the slab (Fig 4(c)). The slab finally begins to drop into the lower mantle at the corner of the slab (Fig 4(d)). We call this type of avalanche a “cold-plume” avalanche in accordance with Maruyama (1994) because the slab becomes drop-shaped (indicated as A(CP) in Table II). In the stagnation stage, slab bending concentrates in the middle of the slab around the 410-km phase transition (Fig 4 (a)). The yielding does not occur at the tip and the horizontal part of the slab. In the avalanche stage, yielding is generated near the 660-km phase transition.

In Cases 5 and 6, the viscosity reduction causes the avalanche of the stagnant slab. This is opposite to the result that the slab maintains stagnation above the 660-km phase boundary for Cases 3 and 4. In these cases, the lower mantle slab viscosity is truncated at 10^{25} Pa·s, so that the slab preserves its stiffness. The lower viscosity of the slab enhances the slab instability as well as generates the stagnation. The fluid dynamical aspects will be analyzed in the next subsection. In both cases, the subducting plate motion maintains a speed of more than 5 cm yr^{-1}.

A snapshot for Case 7 when the viscosity in the transition zone slab is truncated at 10^{23} Pa·s and the viscosity in the lower mantle slab is identical to that in the ambient mantle is shown in Fig. 3 (e). In this case, the slab generates the “shape-memory” stagnation accompanied by the avalanche. The evolution of this model is shown in Fig. 5. The subducted lithosphere forms the stagnant slab hanging beneath the 660-km phase transition because the lower viscosity of the slab has a weaker shape memory compared to Case 5. Once the horizontally wide slab is formed, the tip of the slab can descend sluggishly. The slab therefore behaves as a “stagnant” slab. During slab stagnation, the slab migrates backward. The speed of slab retreat is fastest in the stagnant slab formation stage, that is, the large slab deformation.

In “shape-memory” slab stagnation, the 660-km phase transition cannot completely block the slab penetration and the slab finally drops into the lower mantle. In Case 5, the slab finally penetrates into the lower mantle with the “cold-plume” avalanche. In Case 7, the slab maintains its shape during the avalanche because the tip of the slab does not cross the 660-km phase boundary (Fig. 4 (c), (d)). We call this type of the slab penetration the “shape-memory” avalanche (indicated as A(SM) in Table II). In this stage, the moving plate velocity reaches 10 cm yr^{-1}. The viscosity increase in the lower mantle due to the pressure dependence does not decelerate the plate motion because the low viscosity prevents the lower mantle slab from behaving as a stress guide. Trench retreat no longer occurs, but trench advance is begun. At the same time, the overriding plate still moves in the opposite direction against the trench migration because the wedge mantle flow induced by the slab descent drags the overriding plate. Snapshots of the whole area of the model are shown in Fig. 6. The effect of the wedge mantle flow induced by the developed slab is strong enough to generate compressional stress even when the trench moves backward during the slab stagnation (Fig. 7). Especially during slab penetration, the back-arc lithosphere becomes strongly compressional (Fig. 6).

In Cases 8 and 9, the slab beneath the 410-km phase transition has a viscosity of 10^{22} Pa·s with a γ_{660} of -3 MPa K^{-1}. In both cases, “phase-buoyancy” stagnation is generated. The final state for Case 8 with the density contrast of 100 % olivine composition is shown in Fig. 3 (f). Slab softening induces the slab instability in the middle of the stagnant slab. A similar style of this instability is found in the results for the cases with a soft slab in Christensen (1996).

We examine the effect of grain-size reduction expressed by Eqs. (1), (3), (4) and (5) at the phase transition to compare the cases with viscosity truncation. We assume the threshold temperature at which the grain size is reduced almost in the whole portion of the lower mantle slab (Ito and Sato, 1991; Karato et al, 1995; Kubo et al., 2000). In Case 10 (γ_{660} = -2 MPa K^{-1}), the evolution is similar to the case without viscosity reduction (Case 2, Fig 3 (a)). The buoyancy of the phase transition is less effective than that in Case 5 because of the higher viscosity of the lower mantle slab. The slab lies horizontally at a 1000-km depth because of the pressure-dependent viscosity. Because of the viscosity reduction in the lower mantle, the plate motion is not decelerated as in Case 2. The faster subduction supplies a larger amount of the cold lithosphere into the lower mantle so that the lower mantle slab becomes thicker than that of Case 2. In Case 11 (γ_{660} = -3 MPa K^{-1}), the slab temporarily stagnates at the 660-km phase transition. The slab finally penetrates into the lower mantle as Case 5 does. The structure of the stagnant slab is between those of Cases 5 and 6. A model without viscosity truncation in the upper mantle and with the viscosity truncation in the lower mantle provides a good approximation for the model with grain-size reduction.

3.2 Force balance and instability of the stagnant slab

To explain the obtained slab structure, here we consider forces working on the stagnant slab and the stability of the slab above the 660-km phase transition. For simplicity, we examine the stability of the stagnant slab as a 1-D Rayleigh-Taylor instability problem. Because a stationary stagnant slab is considered, we neglect the forces generated by slab motion such as viscous resistance from the ambient mantle. The forces acting on the stagnant slab are shown in Fig. 9. The forces consist of the following: (1) descending slab load, which is a force with which the descending slab pushes down the stagnant slab (f_s); (2) stagnant slab buoyancy, or the negative buoyancy of the stagnant slab (f_n); (3) rollback slab hanging, a force with which the trench retreat pulls up the stagnant slab (f_t); and (4) phase boundary buoyancy, which is the positive buoyancy of the 660-km phase transition (f_P). Only the vertical components of the forces working on the stationary stagnant slab are considered in the 1-D model.

The force f_s is generated by deformation of the inclined part of a slab because of the descending motion. The z-component f_{sz} is written as

$$f_{sz} = 2\delta\eta_s \frac{u_s}{h_u}\sin^2\theta \quad , \qquad (12)$$

where is η_s the effective viscosity of the slab including the yielding, and u_s is the velocity of the subducting plate motion. The stagnant slab buoyancy force f_n is written as

$$f_n = \rho_0 \alpha \Delta T_s g \delta l_s \, , \qquad (13)$$

where δ is the thickness of the slab, ΔT_s is the mean slab temperature difference from that of the ambient mantle and l_s is the length of the stagnant slab. The force f_t is generated by the slab deformation because the trench retreat extends a distance from the trench to the point where the downward moving slab connects to the stagnant slab. The z-component f_{tz} is written as

$$f_{tz} = 2\delta\eta_s \frac{u_t}{h_u} \cos\theta \sin^2\theta \tag{14}$$

The forces f_P is expressed as

$$f_p = -\frac{\gamma_{660}\Delta\rho_{660}\Delta T_s l_s}{\rho_0} \quad . \tag{15}$$

Among these forces, f_s and f_n promote slab penetration into the lower mantle. On the contrary, f_p and f_t prevent slab penetration. Because of the high viscosity of the slab, f_s and f_t are larger than the others. If the trench retreat does not occur, the slab can easily penetrate because f_s is much larger than f_p. Only f_t can resists f_s so that the trench retreat is essential for generating the stagnant slab. Because of this, the stress at the slab tip does not reach the yield stress in the stagnation stage in our numerical models (Fig 4 (a)). Trench retreat is necessary to generate the stagnant slab, as several previous studies have reported (Christensen, 1996; Čížková et al., 2002; Tagawa et al., 2007a; Torii and Yoshioka, 2007; Fukao et al., 2009).

To explain the viscosity effects on the avalanche of the stagnant slab, we consider the growth time of the Rayleigh-Taylor instability of the stagnant slab. The growth time is written as the quotient of the effective viscosity and the characteristic stress scale,

$$\tau_{RT} \sim \frac{\eta_e}{\sigma_e} \quad , \tag{16}$$

where σ_e is the vertical stress of the stagnant slab, which is calculated from the quotient of the summation of forces and the stagnant slab length, written as

$$\sigma_e = \frac{f_n - f_p + f_{sz} - f_{tz}}{l_s} \quad . \tag{17}$$

It is appropriate to consider that the effective viscosity η_e is set to be that of the lower mantle for the "shape-memory" avalanche, and to the slab viscosity for the "cold-plume" avalanche. The growth time τ_{RT} is therefore proportional to the viscosity of the stagnant slab for the "cold-plume" avalanche. The "cold-plume" avalanche can also be referred to as the "Rayleigh-Taylor" avalanche. The higher the transition zone slab viscosity is, the longer the growth time is. Because the viscosity has yield stress dependence, it is difficult to calculate the slab viscosity. Additionally, the magnitudes of these forces are expected to be orders of magnitude different because of the viscosity contrast between the slab and the surrounding mantle. It is therefore difficult to precisely estimate σ_e. We can however roughly determine that σ_e is of the same range spanned by the stress caused by the phase boundary buoyancy and that due to the yield stress (~ 100 MPa). When we use $\Delta\rho_{660} / \rho$ of 0.06, γ of -3 MPa K^{-1} and ΔT_s of 500 K, we find that σ_e is about 10 MPa. In the case with high viscosity, τ_{RT} becomes more than 10^9 years so that the slab continues to stagnate above the 660-km phase transition. On the other hand, when the slab viscosity is 10^{22} Pa·s with σ_e of 10 MPa, τ_{RT} is estimated to be about 3×10^7 years. The slab can penetrate into the lower mantle with an observationally reasonable geological time scale before the slab is thermally assimilated into the ambient mantle.

4. Discussion

We revealed the dynamical mechanism for slab stagnation and avalanche by examining how slab rheology controls the deformation of the subducted lithosphere interacting with the phase transitions. The stagnant slab is generated in two ways: with "phase-buoyancy" stagnation and "shape-memory" stagnation. In the former case, the positive buoyancy of the 660-km phase transition dominates the slab structure. The stagnant slab is formed above the 660-km phase transition. The slab tip is sometimes floating at a few tens to 100 km above the 660-km phase boundary. In the latter case, the plasticity of the slab generates a horizontally elongated shape that causes the slow descent of the slab end. In this case, even the slab stagnating beneath the 660-km phase transition is produced. The shape-memory effect due to the high viscosity of the slab coupled with the phase boundary buoyancy has an important role in producing the stagnant slab at various depths (Fukao et al., 2009). This is one of the important aspects in this study.

We have pointed out the dynamics of how slab backward migration generates a stagnant slab based on force balance analysis for the statically stagnant slab. Because of the large viscosity, the slab places the total load of its negative buoyancy on the phase transition. The trench retreat is important in promoting the slab stagnation because of the following two reasons: (1) Trench retreat lessens the dip of the subducted slab so that it reduces the descending slab load (Eq. (12)). (2) Trench retreat induces the hanging force (Eq. (14)) of the stagnant slab to balance with the descending slab load. Phase transition with a very large absolute value of the Clapeyron slope (Christensen, 1984; Davies, 1995; Čížková et al., 2002; Tagawa et al. 2007a), or substantial slab viscosity reduction is required to produce the slab stagnation without the trench retreat,

The slab viscosity also controls the slab penetration into the lower mantle, and not only the slab stagnation. This can be explained by the growth time of the gravitational (Rayleigh-Taylor) instability proportional to the slab viscosity. This means that the slab stagnates more easily at the phase boundary, that is, the low viscosity slab finally develops into an avalanche. The most extreme case of this is that in constant or laterally uniform viscosity convection. In this case, the growth time of the instability becomes shorter than in the case with temperature-dependent viscosity. This is the reason why intermittent mixing (Machetel and Weber, 1991; Honda et al, 1993; Tackley et al., 1993) is often observed in constant or laterally uniform viscosity convection. When the slab has a viscosity as large as 10^{25} Pa·s, the growth time becomes much longer than the thermal assimilation time of the thermal diffusion. In this case, the stagnant slab cannot be expected to penetrate into the lower mantle. If the effective slab viscosity is on the order of 10^{22} to 10^{23} Pa·s, the growth time becomes tens of millions of years. This value is consistent with the duration of stagnation estimated from the stagnant slab volume derived by seismic waveform analysis (Tajima and Grand, 1998). The existence of deep focus earthquakes may imply rigid slabs in the mantle transition zone. If this is the case, viscosity reduction due to the 660-km phase transition (Ito and Sato, 1991; Karato et al., 1995; Kubo et al., 2000) is a plausible mechanism that would enhance the avalanche of stagnant slabs, as our models (Cases 5 and 6) showed. Results from seismic waveform studies are consistent with this scenario, in which penetration begins at the hinge of the stagnant slab (Li and Yuan, 2003; Li et al., 2008). Geoid anomalies indicate extinction of lateral viscosity variations in the lower mantle (Zhong and Davies, 1999; Yoshida and Nakakuki, 2008). The other candidate for a slab avalanche would be trench advance induced by overriding plate motion forced by the surrounding plates or intensifying the coupling at the plate boundary (Sobolev and Babeyko, 2005). In our stability analysis, we neglect the effect of viscous resistance from the ambient mantle. The viscosity jump at the 660 km phase boundary is expected to significantly increase the viscous resistance. Previous studies pointed out that the viscosity jump promotes the slab stagnation (Christensen, 1996; Torii and Yoshioka, 2007; Fukao et al., 2009).

We have also shown the mutual interaction between trench migration and slab evolution in the transition zone. Slab stagnation promotes backward trench migration as previous numerical (Tagawa et al., 2007a) and analog (Kincaid and Olson, 1987) simulations have shown. When the lower mantle slab does not lose its stiffness, deformation of the high viscosity slab is necessary to continue subduction because the pressure-dependent viscosity increases viscous resistance of the lower mantle. In this case, trench retreat continues after slab penetration. In models with a low viscosity slab in the lower mantle, deformation in the high viscosity part of the slab is not substantial during the slab penetration stage. In this case, trench advance occurs during slab penetration. It is therefore reasonable to understand trench migration as a process that supplies energy for slab deformation from the potential energy release due to the vertical descent of the inclined slab. This dynamic feedback mechanism would explain the relationship between slab stagnation/penetration and the trench rollback/advance in the Izu-Bonin-Mariana trench (van der Hilst and Seno, 1993; Miller et al, 2005).

We neglected several geodynamical effects to focus on the slab rheology effects on slab dynamics in the transition zone. The most characteristic simplification of our simulations is that we employed an initiating subduction model with 2-D Cartesian geometry including phase transitions to model the slab's interaction with the mantle transition zone. In order to realize trench migration controlled dynamically, the free-slip boundary condition is employed. Because the 3-D density structure of the slab controls plate motion, the slab is partly pushed or pulled from the connected surface plate. From seismic observations, some slabs (Izu-Bonin and Tonga-Kermadic slabs) have down-dip compressional stress in the shallow part, and the others have tensional or neutral stress (Isacks and Molnar, 1971). The slab buoyancy load in a 2-D model with a free-slip surface boundary would be underestimated for the compressional slab. Effects of the ambient mantle flow, which reflects the history of the mantle convection, should not be neglected when we examine the slab dynamics comparing observed tectonic features. For example, Gurnis et al. (2000) pointed out the interaction of the subducting Tonga slab with an ascending plume. Three-dimensional spherical geometry is also expected to control slab dynamics with trench migration (Yamaoka, 1988). Stegman et al. (2006) and Schellart et al. (2007) reported that the length of the trench controls the backward motion of the subducted slab. Pressure from the lateral mantle flow on the slab (Billen, 2008) is also neglected in our analysis of the stagnant slab. This may significantly influence both the dip angle and the trench migration of the slab to affect on the slab stagnation and avalanche.

We also reiterate that we assumed or simplified several physical properties that affect slab rheology and buoyancy, such as yield stress (Čížková et al., 2002), viscosity truncation for the lithosphere, function of the viscosity decrease due to grain-size reduction, composition of the lithosphere (Christensen, 1997), and buoyancy due to metastable olivine (Schmeling et al, 1999). A simulation with wider rheological parameters incorporating the compositionally layered lithosphere should be performed next to examine the effects on slab deformation.

5. Conclusion

We performed numerical simulation of slab interactions with the mantle transition zone using dynamical models of the integrated plate-mantle system to understand the mechanics for formation and avalanche of the stagnant slab and dynamical feedbacks to the surface tectonics. The points of our study are summarized as follows:

(1) We find two types of slab interaction with the 660-km phase boundary: "phase-buoyancy" stagnation and "shape-memory" stagnation. In the former case, the slab stagnates above the 660-km discontinuity because of the positive buoyancy of the phase transition. In the latter case, the plasticity of the slab forms a horizontal slab at or beneath the phase transition. The shape-memory effect coupled with the phase boundary buoyancy causes diverse structures of the stagnant slab at various depths.

(2) The slab viscosity also determines the fate of the subducted plate. The viscosity reduction due to slow grain growth causes the slab penetration. This effect is opposite to that of stagnation.

(3) The stability analysis of the stagnant slab explains mechanisms in which trench migration generates slab stagnation and the viscosity reduction at the 660-km phase transition induces the slab penetration.

(4) The trench retreat and advance related to slab stagnation and avalanche are reproduced. Trench retreat can be understood as a process of energy supply to the slab stagnation from the gravitational potential energy generated by vertical descent of the subducting slab.

Acknowledgement

The authors thank Drs. M. Billen and T. Nakagawa for their helpful review and comments for improving the manuscript. Most of the figures were drawn using the “Generic Mapping Tools (GMT)” software package (Wessel and Smith, 1998). This study is supported by the Grants-in-Aid for Scientific Research “Stagnant Slab Project” (No. 1675207) from the Ministry of Education, Culture, Sports, Science and Technology, Japan.

References

Akaogi, M., Ito, E., Navrotsky, 1989. A., Olivine-modified spinel-spinel transitions in the system Mg_2SiO_4-Fe_2SiO_4: Calorimetric measurements, thermochemical calculation, and geophysical application, J. Geophys. Res., 94, 15671-15685.

Billen, M. I., 2008. Modeling the dynamics of subducting slab, Ann. Rev. Earth Planet. Sci., 36, 325-356.

Byerlee, J., 1978. Friction of rocks. Pure Appl. Geophys. 116, 615-626.

Christensen, U., 1984. Convection with pressure- and temperature-dependent non-Newtonian rheology, Geophys. J. R. Astron. Soc., 77, 343-384.

Christensen, U. R., 1996. The influence of trench migration on slab penetration into the lower mantle, Earth Planet. Sci. Lett., 140, 27-39.

Christensen, U. R., 1997. Influence of chemical buoyancy on the dynamics of slabs in the transition zone, J. Geophys. Res., 102, 22435-22443.

Christensen, U. R., Yuen, D. A., 1984. The interaction of a subducting lithospheric slab with a chemical or phase boundary, J. Geophys. Res., 89, 4389-4402.

Christensen, U. R. Yuen, D. A., 1985. Layered convection induced by phase transitions, J. Geophys. Res., 90, 10291-10300.

Čížková, H., van Hunen, J., van den Berg, A. P., Vlaar, N. J., 2002 The influence of rheological weakening and yield stress on the interaction of slabs with the 670 km discontinuity, Earth Planet. Sci. Lett., 199, 447-457.

Davies, G. F., 1995. Penetration of plates and plumes through the mantle transition zone, Earth Planet. Sci. Lett., 133, 507-516.

Dziewonski, A. M., Anderson, D. L., 1981. Preliminary reference Earth model, Phys. Earth Planet. Inter., 25, 297-356.

Fei, Y., van Orman, J., Li, J., van Westrenen, W., Sanloup, C., Minarik, W., Hirose, K., Komabayashi, T., Walter, M., Funakoshi, K., 2004. Experimentally determined postspinel transformation boundary in Mg_2SiO_4 using MgO as an internal pressure standard and its geophysical implications, J. Geophys. Res., 109, B02305, doi:10.1029/2003JB002562.

Flanagan, M. P., Shearer, P. M., 1998. Global mapping of topography on transition zone velocity discontinuities by stacking SS precursors, J. Geophys. Res., 103, 2673-2692.

Frohlich, C., 1989. The nature of deep-focus earthquakes, Ann. Rev. Earth Planet. Sci., 17, 227-254.

Fukao, Y., Widiyantoro, S., Obayashi, M., 2001. Stagnant slabs in the upper and lower mantle transition region, Rev. Geophys., 39, 291-323.

Fukao, Y., Obayashi, M., Inoue, H., Nenbai, M. 1992. Subducting slabs stagnant in the mantle transition zone, J. Geophys. Res., 97, 4809-4822.

Fukao, Y., Obayashi, M., Nakakuki, T., Deep Slab Project Group, 2009. Stagnant slab: A review, Ann. Rev. Earth Planet. Sci., 37, 19-46.

Gordon, R. G., 2000. Diffuse oceanic plate boundaries: Strain rate, vertically averaged rheology and constraints with narrow plate boundaries and stable plate interiors, in The history and Dynamics of Grobal Plate Tectonics. Geophys. Monograph Series Vol. 121, pp143-159, ed. Richards, M. A. Gordon, R. G., van der Hilst, R., Am. Geophys. Union, Washington, DC.

Gurnis, M., Ritsema, J., van Heijst, H.-J., 2000. Tonga slab deformation: The influence of lower mantle upwelling on a slab in a young subduction zone, Geophys. Res. Lett., 27, 2373-2376.

Heuret, A., Lallemand, S., 2005. Plate motions, slab dynamics and back-arc deformation, Phys. Earth Planet. Inter., 149, 31-51.

Honda, S., Yuen, D. A., Balachandar, S., Reuteler, D., 1993. Three-dimensional instabilities of mantle convection with multiple phase transitions, Science, 259, 1308-1311.

Honda, S., Nakakuki, T., Tatsumi, Y., Eguchi, T., 2000. A simple model of mantle convection including a past history of yielding, Geophys. Res. Lett., 27, 1559-1562.

Irifune, T., 1993. Phase transitions in the earth's mantle and subducting slabs; Implication for their compositions, seismic velocity and density structure and dynamics, Island arc, 2, 55-71.

Isacks, B. L., Molnar, P., 1971. Distribution of stresses in the descending lithosphere from a global survey of focal-mechanism solutions of mantle earthquakes, Rev. Geophys., 9, 103-174.

Ito, E. and H. Sato, 1991. Aseismicity in the lower mantle by superplasticity of the descending slab, Nature, 351, 140-141.

Iwamori, H., 1998. Transport of H_2O and melting in subduction zones, Earth Planet. Sci. Lett., 160, 65-80.

Karato, S. 1989. Grain growth kinematics in olivine aggregate, Tectonophys., 168, 255-273.

Karato, S., Wu, P., 1993. Rheology of the upper mantle: A synthesis, Science, 260, 771-778.

Karato, S., Zhang, S., Wenk, H.-R., 1995. Superplasticity in the Earth's lower mantle: Evidence from seismic anisotropy and rock physics, Science, 270, 458-461.

Karato, S., Riedel, M. R., Yuen, D. A., 2001. Rheological structure and deformation of subducted slabs in the mantle transition zone: Implications for mantle circulation and deep earthquakes, Phys. Earth Planet. Inter., 127, 83-108.

Katsura, T., Ito, E., 1989. The system Mg_2SiO_4-Fe_2SiO_4 at high pressures and temperatures: Precise determination of stabilities of olivine, modified spinel, and spinel, J. Geophys. Res., 94, 15663-15670.

Katsura, T., Yamada, H., Shinmei, T., Kubo, A., Ono, S., Kanzaki, M., Yoneda, A., Walter, M. J., Ito, E., Urakawa, S., Funakoshi, K., Utsumi, W., 2003. Post-spinel transition in Mg_2SiO_4 determined by high P-T in situ X-ray diffractometry, Phys. Earth Planet. Inter., 136, 11-24.

Kincaid, C., Olson, P., 1987. An experimental study of subduction and slab migration, J. Geophys. Res., 92, 13832-13840.

King, S. D, Ita, J., 1995. Effect of slab rheology on mass transport across a phase transition boundary, J. Geophys. Res., 100, 20211-20222.

Kohlstedt, D. L. Evans, B., Mackwell, S. J., 1995. Strength of the lithosphere: Constraints provided by the experimental deformation of the rocks. J. Geophys. Res., 100, 17587-17602.

Kubo, T., Ohtani, E. , Kato, T., Urakawa, S., Suzuki, A., Kanbe, Y., Funakoshi, K., Utsumi, W., Fujino, K., 2000. Formation of metastable assemblages and mechanisms of the grain-size reduction in the postspinel transformation of Mg_2SiO_4, Geophys. Res. Lett., 27, 807-810.

Li, J., Chen, Q.-F., Vanacore, E., Niu, F., 2008. Topography of the 660-km discontinuity beneath northwest China: Implications for a retrograde motion of the subducting Pacific slab, Geophys. Res. Lett., 35, L01302, doi:10.1029/2007GL031658.

Li, X. Yuan, X., 2003. Receiver functions in northeast China – implications for slab penetration into the lower mantle in northwest Pacific subduction zone, Earth Planet. Sci. Lett., 216, 679-691.

Machetel, P., Weber, P., 1991. Intermittent layered convection in a model mantle with an endothermic phase change at 670 km, Nature, 350, 55-57.

Maruyama, S., 1994. Plume tectonics, J. Geol. Soc. Japan, 100, 24-49.

Miller, M. S., Gorvatov, A., Kennet, B. L. N., 2005. Heterogeneity within the subducting Pacific slab beneath the Izu-Bonin-Mariana arc: Evidence from tomography using 3D ray tracing inversion techniques, Earth Planet. Sci. Lett., 235, 331-342.

Milne, G. A., Mitrovica, J. X., Davis, J. L., 1999. Near-field hydro-isostasy: The implementation of a revised sea-level equation, Geophys. J. Int., 139, 464-482.

Molnar, P., Atwater, T., 1978. Interarc spreading and Cordilleran tectonics as alternates related to the age of subducted oceanic lithosphere, Earth Planet. Sci. Lett., 41, 330-340.

Nakakuki, T., Sato, H., Fujimoto, H., 1994. Interaction of the upwelling plume with the phase and chemical boundary at the 670 km discontinuity: Effects of temperature-dependent viscosity, Earth Planet. Sci. Lett., 121, 369-384.

Nakakuki, T., Hamada, C., Tagawa, M., 2008. Generation and driving forces of plate-like motion and asymmetric subduction in dynamical models of an integrated mantle-lithosphere system, Phys. Earth Planet. Int., 166, 128-146.

Okuno, J., Nakada, M., 2001. Effects of water load on geophysical signals due to glacial rebound and implications for mantle viscosity, Earth Planets Space, 53, 1121-1135.

Peacock, S. M., 1991. Numerical simulation of subduction zone pressure-temperature-time paths: constrains on fluid production and arc magmatism, Phil. Trans. R. Soc Lond. A, 335, 341-353.

Riedel, M. R., Karato, S., 1997. Grain-size evolution in subducted oceanic lithosphere associated with the olivine-spinel transformation and its effects on rheology, Earth Planet. Sci. Lett., 148, 27-43.

Rubie, D. C., 1984. The olivine→spinel transformation and the rheology of subducting lithosphere, Nature, 308, 505-508.

Schellart, W. P., Freeman, J., Stegman, D. R., Moresi, L., May, D., 2007. Evolution and diversity of subduction zone controlled by slab width, Nature, 446, 308-311.

Schmeling, H., Monz, R., Rubie, D. C., 1999. The influence of olivine metastability on the dynamics of subduction, Earth Planet. Sci. Lett., 165, 55-66.,

Schubert, G., Turcotte, D. L., Olson, P., 2001. Mantle convection in the Earth and planets, 956 pp, Cambridge University Press.

Sdrolias, M., Müller, R. D., 2006. Controls on back-arc basin formation, Geochem. Geophys. Geosyst., 7, Q04016, doi:10.1029/2005GC001090.

Seno, T., Maruyama, S., 1984. Paleographic reconstruction and origin of the Philippine Sea, Tectonophys., 102,53-84.

Shito, A., Shibutani, T., 2001. Upper mantle transition zone structure beneath the Philippine Sea region, Geophys. Res. Lett., 28, 871-874.

Shimojuku, A., Kubo, T., Ohtani, E., Yurimoto, H., 2004. Silicon self-diffusion in wadsleyite: Implications for rheology of the mantle transition zone and subducting plates, Geophys. Res. Lett., 31, L13606, doi:10.1029/2004GL020002.

Sobolev, S. V., Babeyko, A. Y., 2005. What drives orogeny in the Andes, Geology, 33, 617-620.

Stegman, D. R., Freeman, J., Schellart, W. P., Moresi, L., May, D., 2006. Influence of trench width on subduction hinge retreat rates in 3-D models of slab rollback, Geochem. Geophys. Geosyst. (G3), 7, Q03012, doi:10.1029/2005GC001056.

Tackley, P. J., 1995. Mantle dynamics: Influence of the transition zone, Rev. Geophys., 33, 275-282.

Tackley, P. J., Stevenson, D. J., Glatzmaier, G. A., Schubert, G., 1993. Effects of an endothermic phase transition at 670 km depth in a spherical model of convection in the Earth's mantle, Nature, 361, 699-704.

Tagawa, M. Nakakuki, T., Tajima, F., 2007a. Dynamical modeling of trench retreat driven by the slab interaction with the mantle transition zone, Earth Planets Space, 59, 65-74.

Tagawa, M., Nakakuki, T., Kameyama, M., Tajima, F., 2007b. The role of history-dependent rheology in plate boundary lubrication for generating one-sided subduction, Pure Appl. Geophys., 164, 879-907.

Takewaki, H., Nishiguchi, A., Yabe, T., 1985. Cubic interpolated pseudo-particle method (CIP) for solving hyperbolic-type equations, J. Comp. Phys., 61, 261-268.

Tajima, F., Grand, S. P., 1998. Variation of transition zone high-velocity anomalies and depression of 660 km discontinuity associated with subduction zones from the southern Kuriles to Izu-Bonin and Ryukyu, J. Geophys. Res., 103, 1501515036.

Tonegawa, T., Hirahara, K., Shibutani, T., 2005. Detailed structure of the upper mantle discontinuities around the Japan subduction zone imaged by receiver function analyses, Earth Planets Space, 57, 5-14.

Torii, Y., Yoshioka, S., 2007. Physical conditions producing slab stagnation: Constrains of the Clapeyron slope, mantle viscosity, trench retreat, and dip angles, Tectonophys, 445, 200-209.

van der Hilst, R., Seno, T., 1993. Effects of relative plate motion on the deep structure and penetration depth of slabs below the Izu-Bonin and Mariana island arcs, Earth Planet. Sci. Lett., 120, 395-407.

van der Hilst, R., Engdahl, E. R., Spakman, W., Nolet, G., 1991. Tomographic imaging of subducted lithosphere below northwest Pacific island arcs, Nature, 353, 3743.

Wessel, P., Smith, W. H. F., 1998. New, improved version of the Generic Mapping Tools released, EOS Trans. Am. Geophys. Union, 79, 579.

Yamaoka, K., 1988. Spherical shell tectonics: on the buckling of the lithosphere at subduction zones, Tectonophys., 147, 179-191.

Yamazaki, D., Inoue, T., Okamoto, M., Irifune, T., 2005. Grain growth kinetics of ringwoodite and its implication for rheology of the subducting slab, Earth Planet. Sci. Lett., 236, 871-881.

Yoshida, M. Nakakuki, T., 2008. Effects on the long-wavelength geoid anomaly of lateral viscosity variations caused by stiff subducting slabs, weak plate margins and lower mantle rheology, Phys. Earth Planet. Int., 172, 278-288.

Zhong, S., Davies, G. F., 1999. Effects of plate and slab viscosities on the geoid, Earth Planet. Sci. Lett., 170, 487-496.

Zhong S., Gurnis, M., 1997. Dynamic interaction between tectonic plates, subducting slabs, and the mantle, Earth Interactions, 1, 1-81.

Figure captions

Fig. 1

A schematic illustration of the model configuration. The dark areas in the uppermost area show subducting and overriding plates. A segment with history-dependent yield strength (areas 2 and 3) is introduced to generate the plate boundary. The star shows the location of first yielding. The low viscosity zone is incorporated into the top right corner to produce freedom for the overriding plate motion. The numbered areas are as follows. 1: Weak zone due to melting, 2: oceanic crust layer with history-dependent yielding, 3: fractured segment of 2, 4: hydrous area with weak yield stress and a smaller activation volume, 5: continental crust with buoyancy, 6: a low viscosity area to generate the overriding plate motion, 7: upwelling plume, 8: fixed high temperature area for the upwelling plume, 9: fixed temperature layer, and 10: the area where $d\rho/dx$ of 0 is imposed to avoid gravitational instability of the overriding plate.

Fig. 2

The viscosity-depth (the solid line) and temperature-depth (the dashed line) profile at x = 5000 km in the initial condition. The horizontal axes show the viscosity (bottom) and the temperature (top), and the vertical axis shows the depth.

Fig. 3

Snapshots near the final state for selected models. Each panel shows the surface velocity (the upper graph) and the close-up temperature field around the subduction zone (the lower color map). The horizontal dashed lines show the center of the phase boundaries (Γ_{410}, Γ_{660} =0.5). The horizontal axes show the x-coordinates and the vertical axes show the velocity (upper) or the depth (lower). The velocity is taken to be positive to the right. The unit of the velocity is cm yr^{-1}. The color scale in the bottom right shows the temperature in Celsius degrees. (a) *Case 2*: a pyrolite composition and γ of -3 MPa K^{-1}, (b) *Case 3*: an olivine composition and γ of -2 MPa K^{-1}, (c) *Case 5*: a pyrolite composition, γ of -2 MPa K^{-1}, and viscosity reduction beneath the 660-km phase transition, (d) *Case 6*: the same as Case 5 except a γ of -3 MPa K^{-1}, (d) *Case 7*: the same as Case 5 except a viscosity truncation at 10^{23} Pa·s between the 410- and 660-km phase transitions, (f) *Case 9*: an olivine composition, γ of -3 MPa K^{-1}, and viscosity truncation at 10^{22} Pa·s beneath the 410-km phase transition, (g) *Case 10*: a pyrolite composition and a γ of -2 MPa K^{-1}, a viscosity decrease in the slab due to grain-size reduction derived by the Eq. (10), and (h) *Case 11*: the same as Case 5 except a γ of -3 MPa K^{-1}.

Fig. 4

The evolution of Case 6 at (a) 22.3 Myr, (b) 29.4 Myr, (c) 48.7 Myr, and (d) 60.6 Myr. The top shows the surface velocity (cm yr^{-1}), the middle shows the logarithm of the viscosity in color with temperature in contour lines at 1000, 1200 and 1400°C, and the bottom shows the maximum stress (σ_{II}, MPa) in color and contour lines at each 50 MPa intervals. The meaning of the axes is the same as in Fig. 3. Because of the trench retreat and the buoyancy of the phase transition, the slab stagnates before about 45 Myr. The transition zone slab lies horizontally above the 660-km phase transition ("phase-buoyancy" stagnation). The slab starts to penetrate into the lower mantle at about 48 Myr. The arrows show the location where yielding of the slab occurs.

Fig. 5

The evolution for Case 7 at (a) 21.0 Myr, (b) 24.5 Myr, (c) 28.7 Myr, and (d) 31.2 Myr. The stagnant slab is formed beneath the 660-km phase boundary at 24.5 Myr. The stagnant slab finally drops into the lower mantle, preserving its shape, at 31.2 Myr. The meanings of the graphs, the contours, and the color scales are the same as those of Fig. 4.

Fig. 6

A snapshot of the whole area for Case 7 at 30.8 Myr. The top shows the surface velocity. The middle shows temperature contours at 200°C intervals, and the color scale shows the logarithm of viscosity (Pa·s). The bottom shows the contour lines of the stream function in 10^{-4} m^2 s^{-1} intervals, and the color scale shows the horizontal stress (MPa).

Fig. 7

The stress field around the subduction zone of Case 7 at 24.5 Myr. The color scale shows the stress and the contours show the temperature at 1000, 1200 and 1400 °C. The arrow shows the back-arc lithosphere with the compressional stress.

Fig. 8

The viscosity field around the subduction zone of Case 11 at 40.8 Myr. The color scale shows the viscosity. The contours show the temperature at 900 and 1400 °C, which are the threshold temperatures of the grain-size reduction for the 410-km and 660-km phase transitions, respectively. The arrow indicates the location where the grain-size reduction occurs.

Fig. 9

The forces acting on a stationary stagnant slab. The dark gray area shows the slab with upper mantle phase, the black area shows the slab with lower mantle phase, the light gray area shows the upper mantle, the darker gray below shows the lower mantle, and the white dashed line shows the 660-km phase boundary. The white characters (f_s, f_n) show the forces promoting the penetration and the black ones (f_p, f_t) show those encouraging the stagnation. The symbols for the forces are as follows: f_s: subducting slab load, f_n: negative buoyancy of the stagnant slab, f_p: buoyancy of the 660-km phase transition, and f_t: trench retreat hanging force. The other symbols are d: depression of the phase boundary, h_u: the thickness of the upper mantle, h_l: the thickness of the lower mantle, l_s: the length of the stagnant slab, u_s: velocity of the subducting plate motion, u_t: velocity of the trench migration, δ: the thickness of the slab.

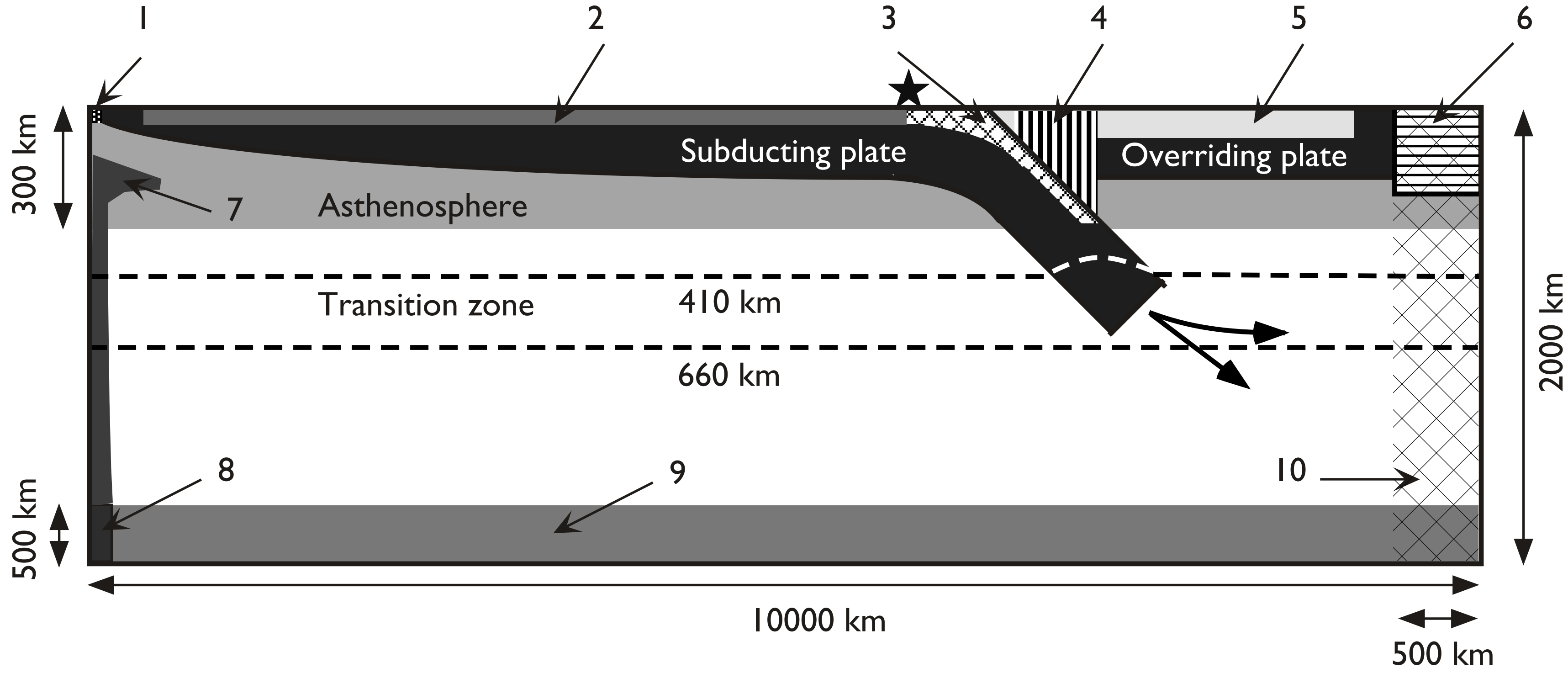
1
2
3
4
5
6
300 km
Subducting plate
Overriding plate
7
Asthenosphere
Transition zone
410 km
660 km
2000 km
8
9
10
500 km
10000 km
500 km

fig. 1

Fig. 2

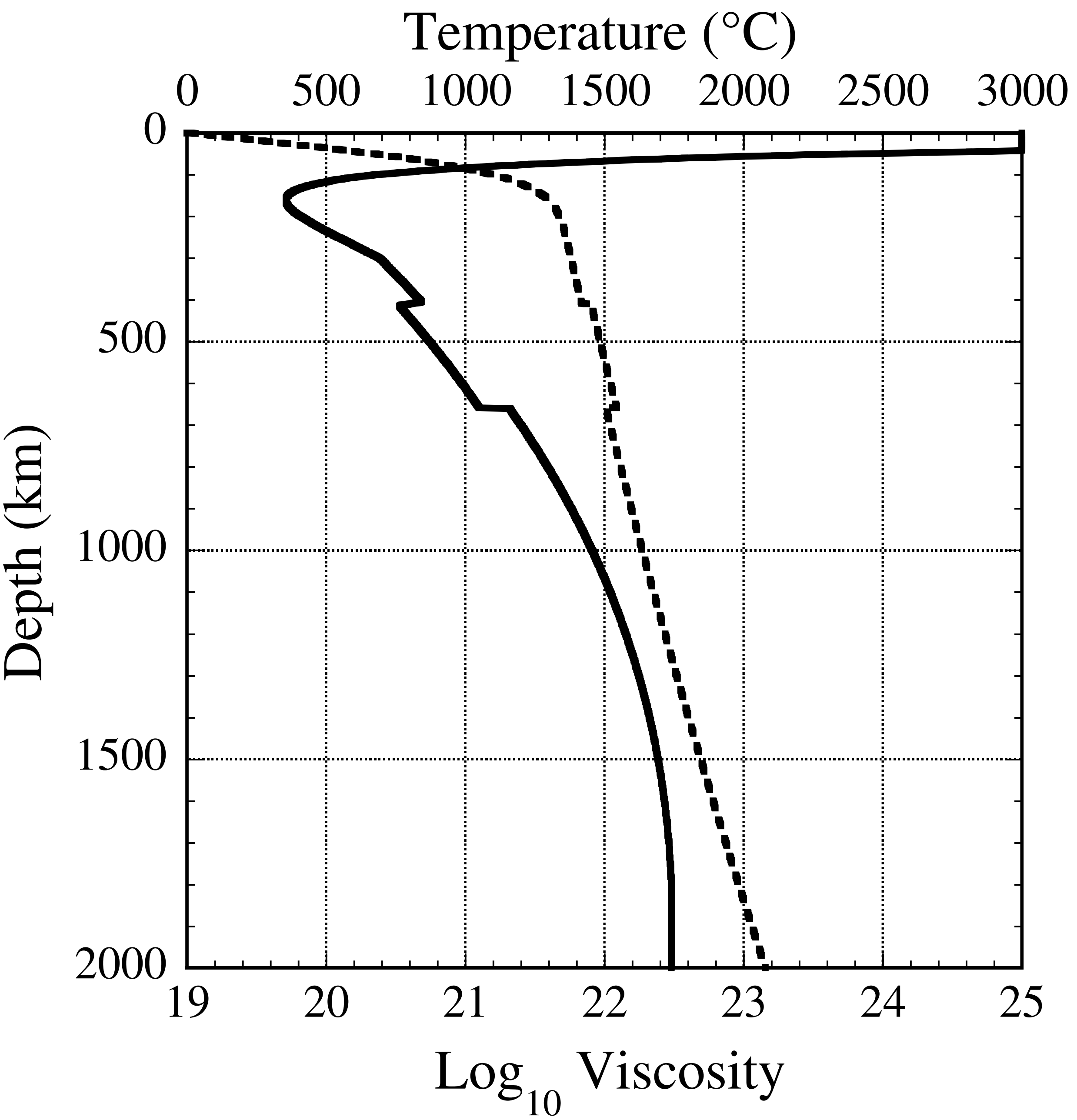

Temperature (°C)
0
500
1000
1500
2000
2500
3000
0
500
1000
1500
2000
Depth (km)
19
20
21
22
23
24
25
Log10 Viscosity

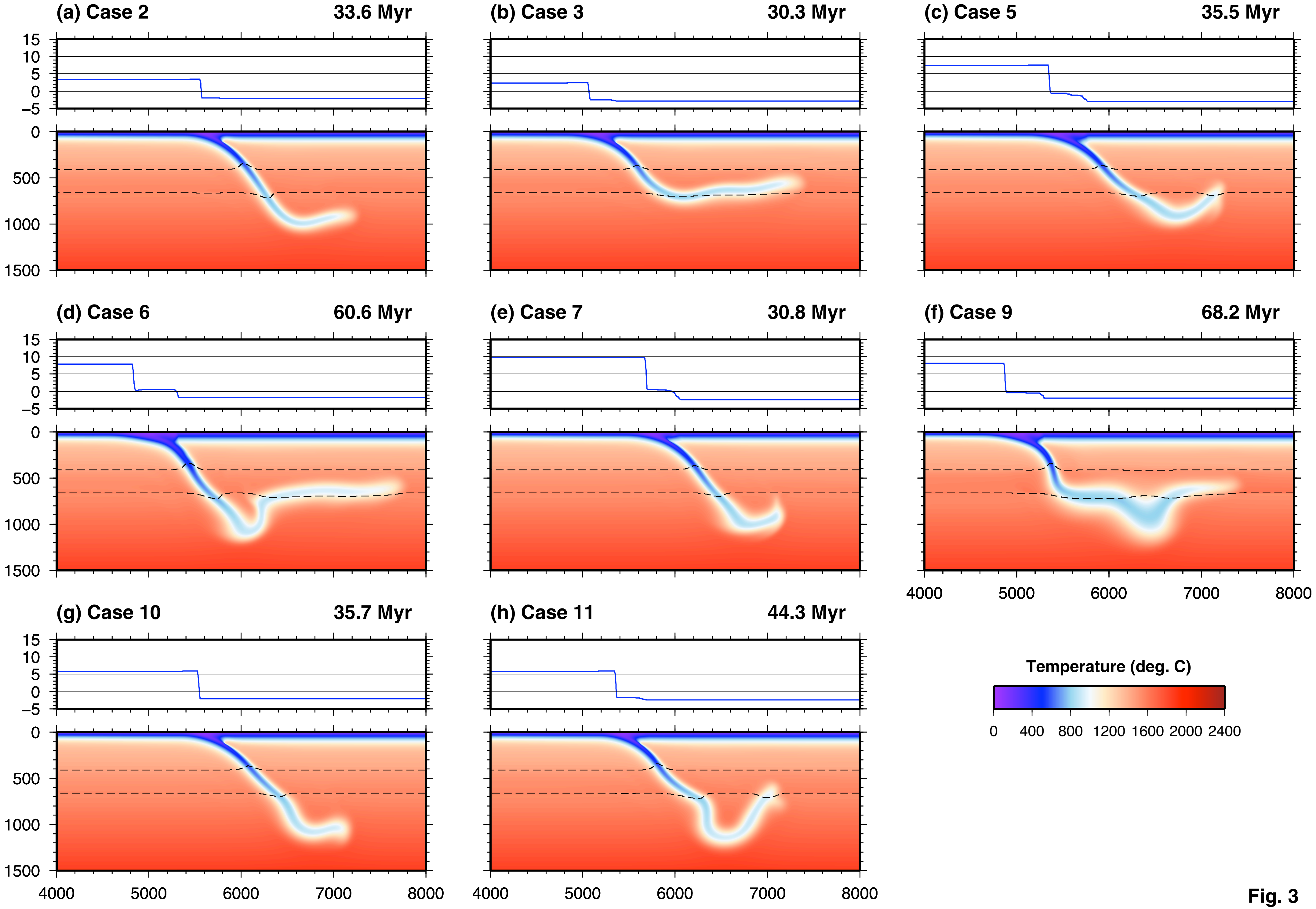
(a) Case 2
33.6 Myr
(b) Case 3
30.3 Myr
(c) Case 5
35.5 Myr
(d) Case 6
60.6 Myr
(e) Case 7
30.8 Myr
(f) Case 9
68.2 Myr
(g) Case 10
35.7 Myr
(h) Case 11
44.3 Myr
15
10
5
0
−5
0
500
1000
1500
4000
5000
6000
7000
8000
Temperature (deg. C)
0
400
800
1200
1600
2000
2400

Fig. 3

Fig.4

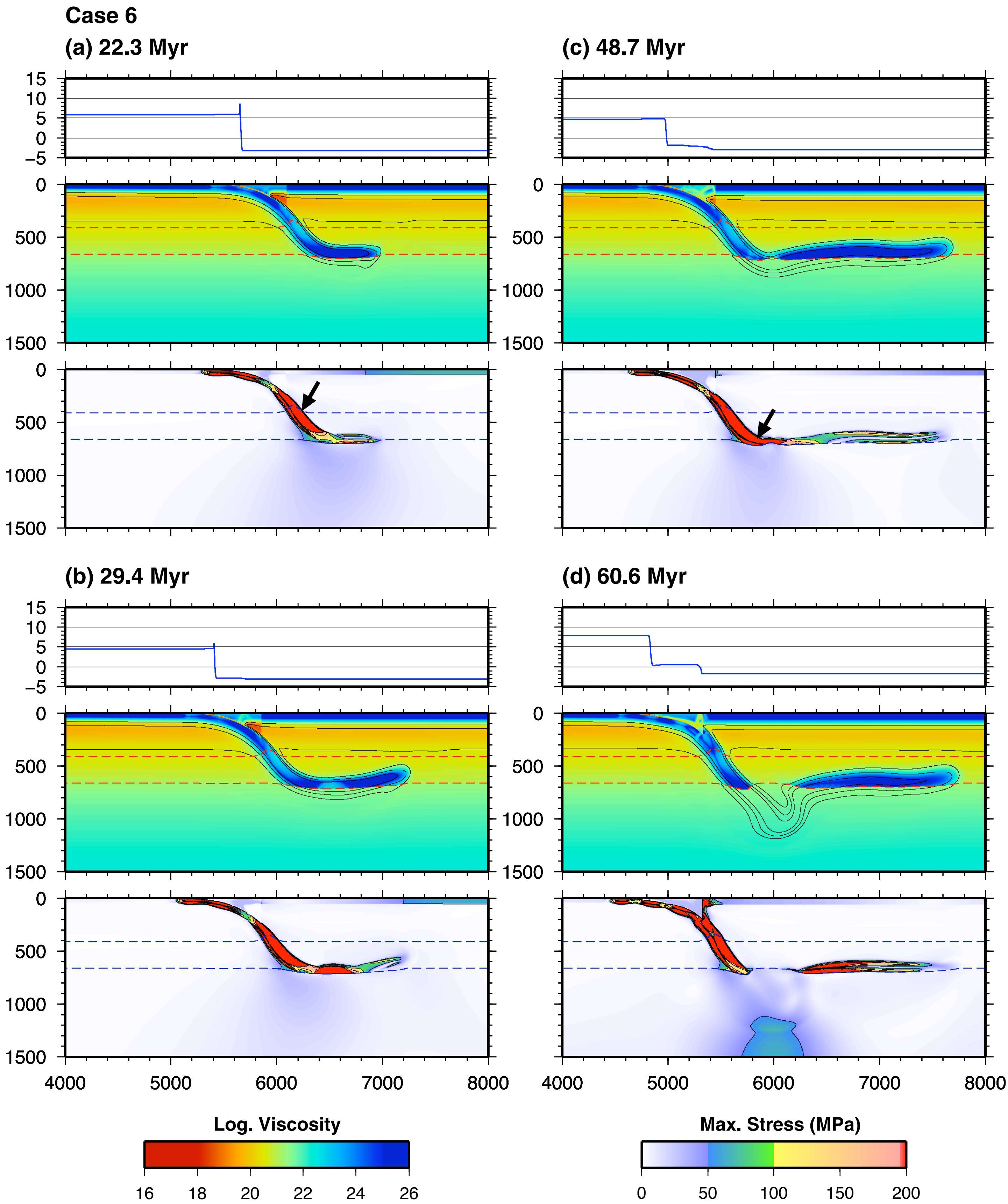

Case 6
(a) 22.3 Myr
(b) 29.4 Myr
(c) 48.7 Myr
(d) 60.6 Myr
Log. Viscosity
16
18
20
22
24
26
Max. Stress (MPa)
0
50
100
150
200

Fig.5

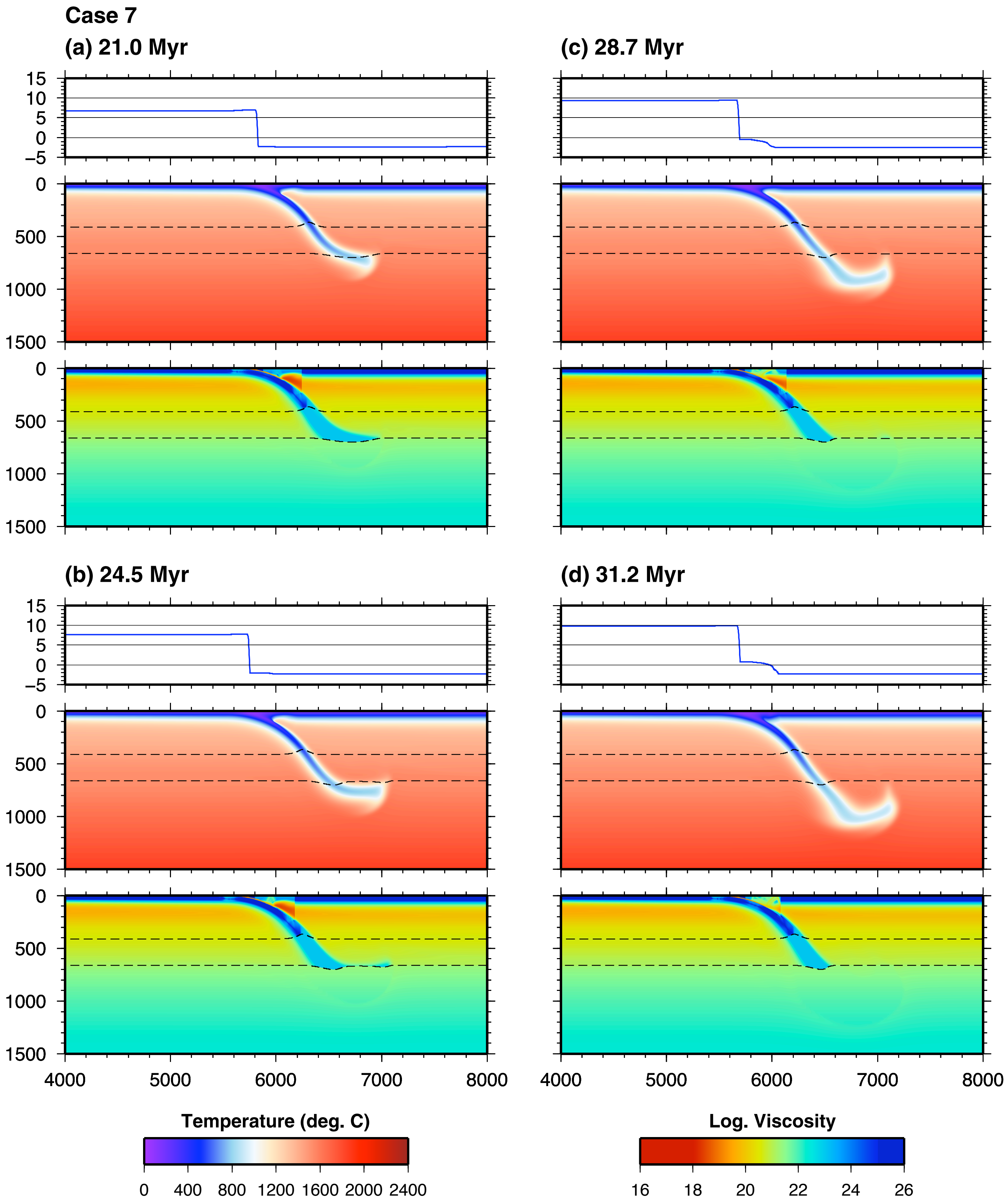
Case 7
(a) 21.0 Myr
(b) 24.5 Myr
(c) 28.7 Myr
(d) 31.2 Myr
15
10
5
0
−5
0
500
1000
1500
4000
5000
6000
7000
8000
Temperature (deg. C)
0
400
800
1200
1600
2000
2400
Log. Viscosity
16
18
20
22
24
26

Fig.6

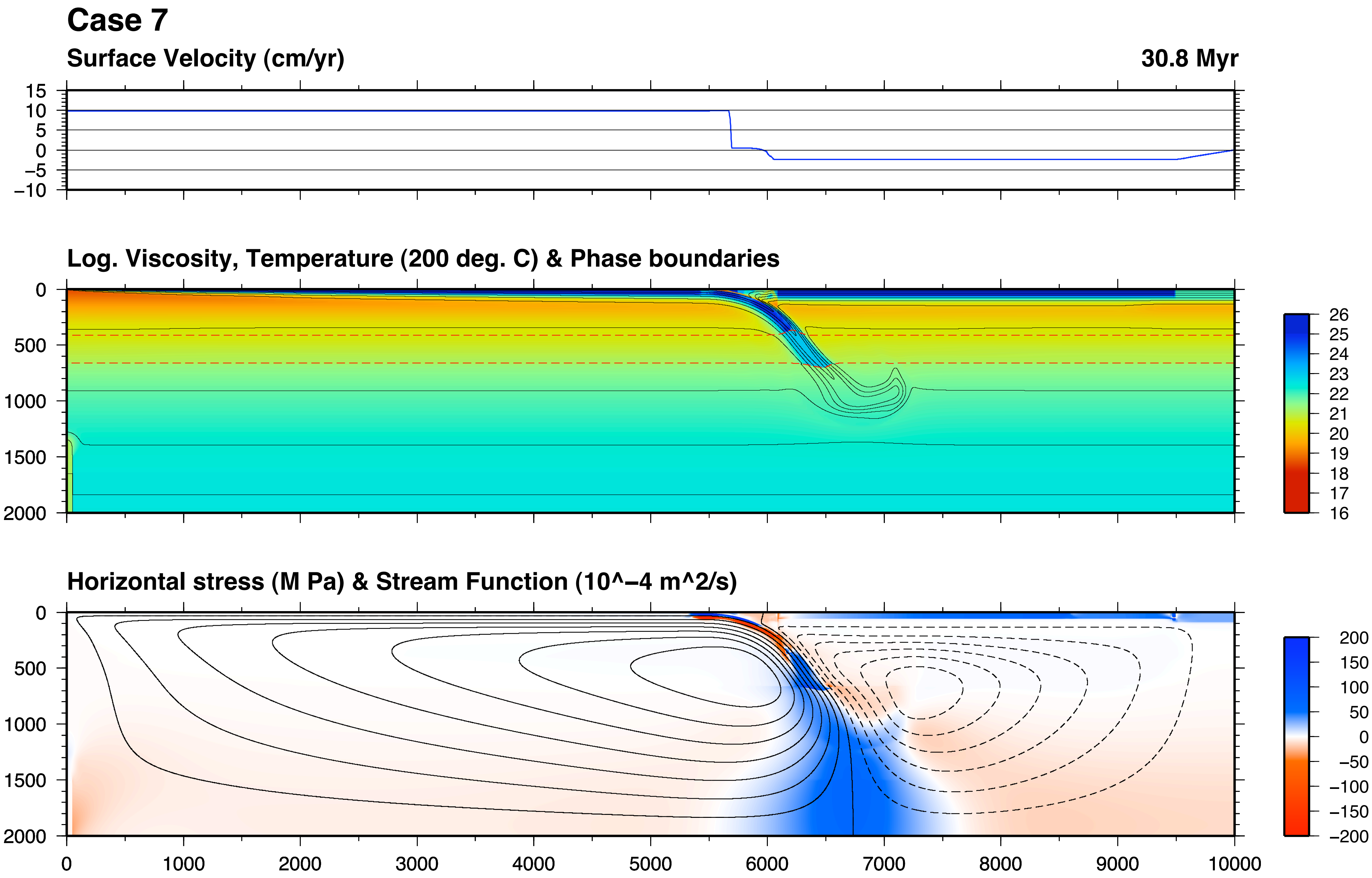
Case 7
Surface Velocity (cm/yr)
30.8 Myr
15
10
5
0
−5
−10
Log. Viscosity, Temperature (200 deg. C) & Phase boundaries
0
500
1000
1500
2000
26
25
24
23
22
21
20
19
18
17
16
Horizontal stress (M Pa) & Stream Function (10^−4 m^2/s)
0
500
1000
1500
2000
200
150
100
50
0
−50
−100
−150
−200
0
1000
2000
3000
4000
5000
6000
7000
8000
9000
10000

Fig.7

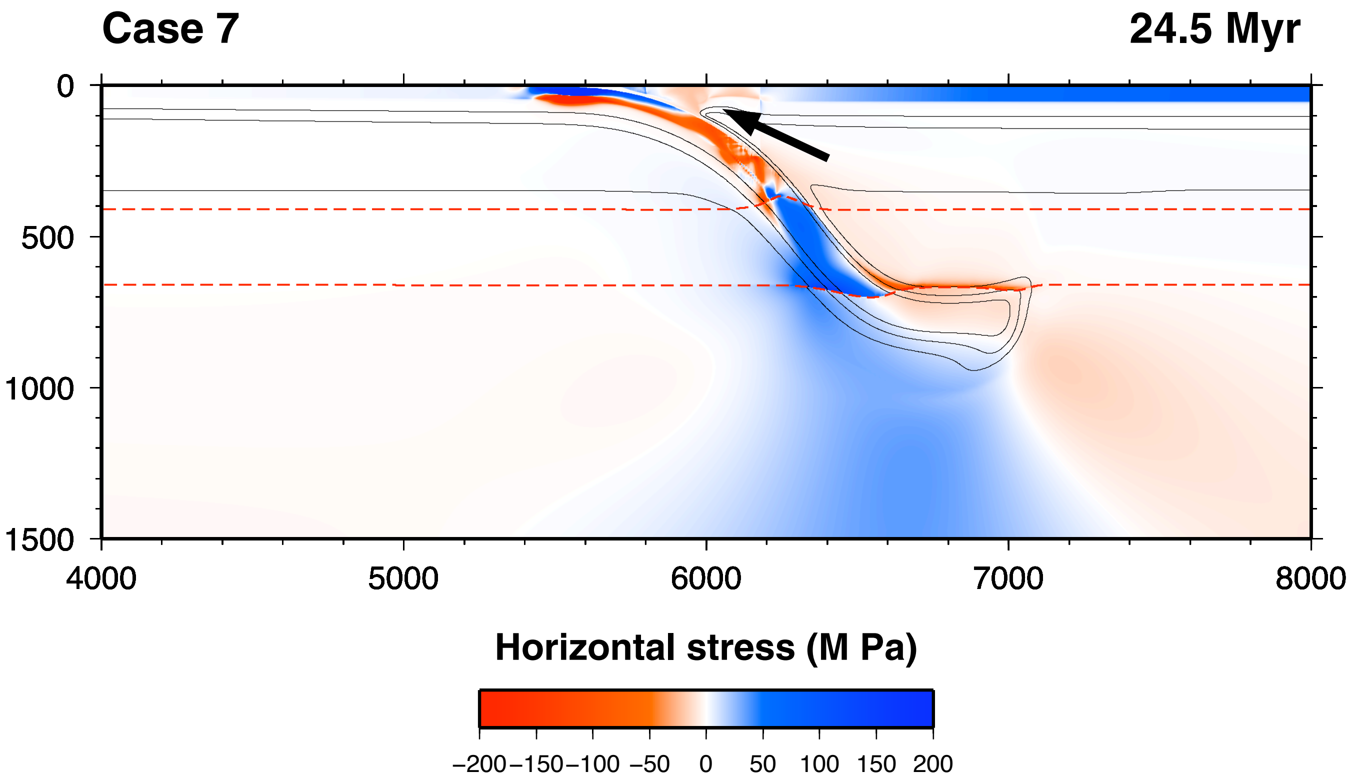
Case 7
24.5 Myr
0
500
1000
1500
4000
5000
6000
7000
8000
Horizontal stress (M Pa)
−200
−150
−100
−50
0
50
100
150
200

Fig.8

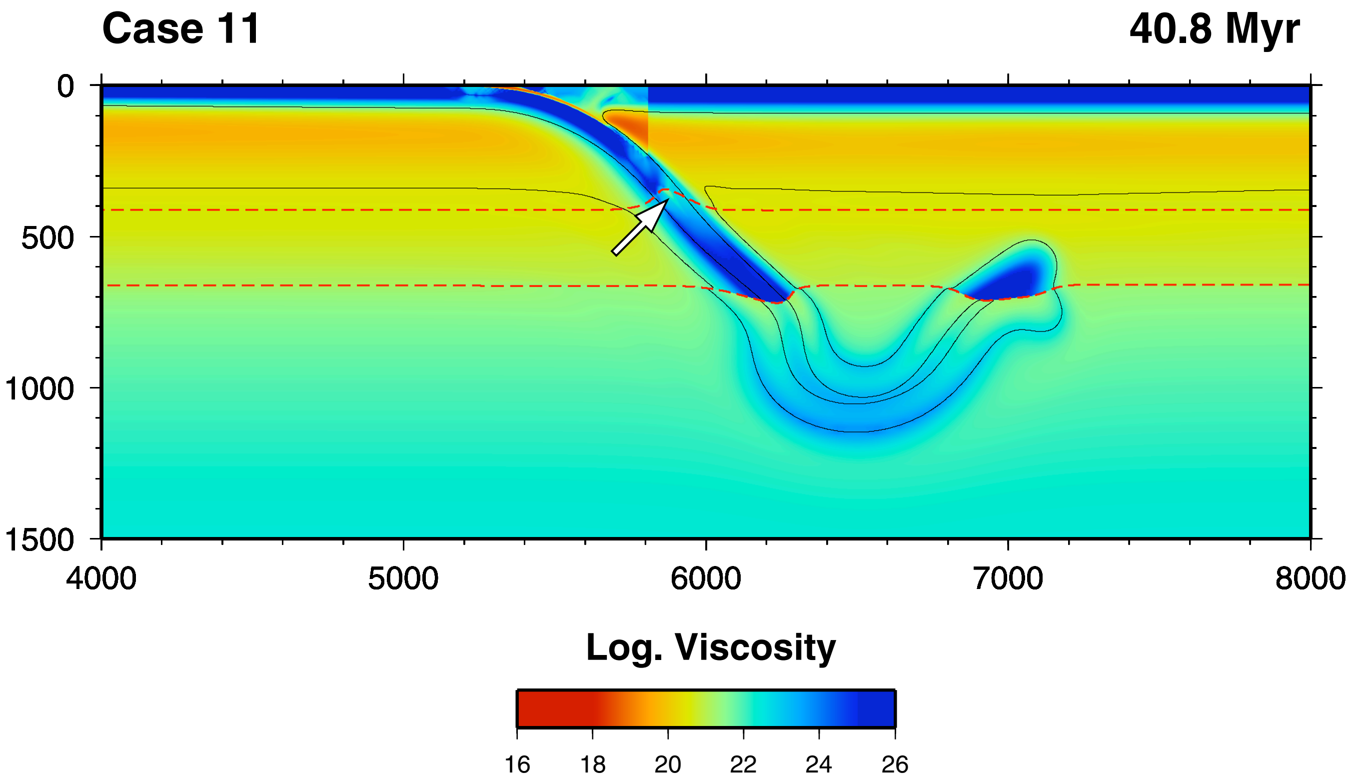

Case 11
40.8 Myr
0
500
1000
1500
4000
5000
6000
7000
8000
Log. Viscosity
16
18
20
22
24
26

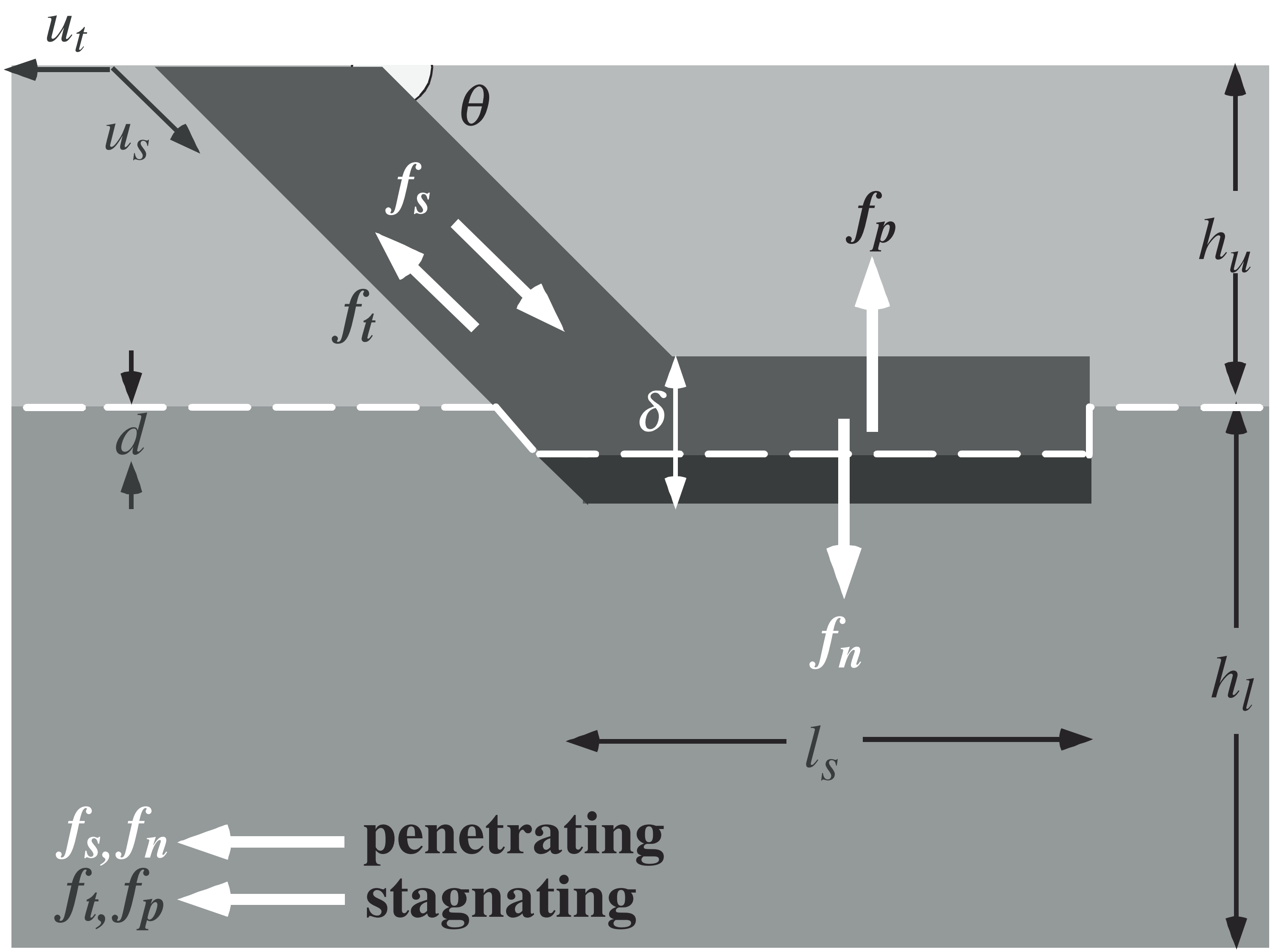
u_t
u_s
θ
f_s
f_t
f_p
h_u
d
δ
f_n
h_l
l_s
f_s, f_n penetrating
f_t, f_p stagnating

fig. 9

Table I: Physical parameters

Symbol	Explanations	Value
A	preexponetial factor	
	in the 0- to 300-km deep layer	2.1484×10^{10} Pa s
	in the 300- to 2000-km deep layer	2.2866×10^{11} Pa s
C_p	specific heat	1.2×10^{3} J K^{-1} kg^{-1}
c_F	friction coefficient of fractured material	0.004
c_Y	friction coefficient of intact material	0.3
d_{410}	half thickness of 410-km phase transition	20 km
d_{660}	half thickness of 660-km phase transition	2 km
d_f	minimum relative grain size	10^{-6}
E^*	activation energy	
	in the 0- to 300-km deep layer	430 kJ mol^{-1}
	in the hydrated area	372.4 kJ mol^{-1}
	in the 300- to 2000-km deep layer	240 kJ mol^{-1}
g	gravity acceleration	10 m s^{-2}
h	thickness of the model	2000 km
H	internal heat source	0 W kg^{-1}
k	thermal conductivity	4.68 W m^{-1}
l	horizontal length of the model	10000 km
n	stress exponent	
	in the 0- to 300-km deep layer	3
	in the 300- to 2000-km deep layer	1
R	gas constant	8.314 J mol^{-1} K^{-1}
T_0	absolute temperature of 0 °C (surface temperature)	273 K
T_{410}	phase transition temperature at 410-km depth	1418 °C
T_{660}	phase transition temperature at 660-km depth	1545 °C
T_c	threshold temperature of the grain-size reduction	
	for the 410-km phase transition	900 °C
	for the 660-km phase transition	1400 °C
T_f	temperature of the minimum grain size	300 °C
T_M	mantle potential temperature	1280 °C

V^*	activation volume	Eq. (2)
V_0	activation volume at z = 0 km	
	in the 0-300 km deep layer	1.5×10^{-5} m^3 mol^{-1}
	in the 300-2000 km deep layer	0.5×10^{-5} m^3 mol^{-1}
V_L	activation volume at z = 2000 km	
	in 0-300 km deep layer	1.5×10^{-5} m^3 mol^{-1}
	in 300-2000 km deep layer	0.4×10^{-5} m^3 mol^{-1}
Y_0	cohesive strength	50 MPa
Y_m	maximum yield strength	
	in the hydrated lithosphere	30 MPa
	in the tip of the continental crust	50 MPa
	in the other segments	200 MPa
z_{410}	depth of 410-km phase transition at T_{410}	410 km
z_{660}	depth of 660-km phase transition at T_{660}	660 km
α	thermal expansivity	2.5×10^{-5} K^{-1}
$\Delta\rho_c$	continental crust-mantle density contrast	600 kg m^{-3}
$\Delta\rho_{410}$	density contrast at the 410-km phase transition	
	for olivine composition model	304.2 kg m^{-3}
	for pyrolite composition model	182.5 kg m^{-3}
$\Delta\rho_{660}$	density contrast at the 660-km phase transition	
	for olivine composition model	323.7 kg m^{-3}
	for pyrolite composition model	194.2 kg m^{-3}
η_{ref}	reference viscosity	5×10^{20} Pa s
η_L	truncated lithosphere viscosity	
	in the transition zone	Varying (Table II)
	in the lower mantle	Varying (Table II)
	in the other lithosphere	1×10^{25} Pa s
ρ_0	reference density	3900 kg m^{-3}
ρ_S	density at the surface	3300 kg m^{-3}

Table II: Cases and varying parameters

Case	Density	γ_{410} MPa/K	γ_{660} MPa/K	TZ[*1] slab η_L Pa·s	LM[*2] slab η_L Pa·s	Slab type[*3]
1	pyrolite	+2	-2	10^{25}	10^{25}	P
2	pyrolite	+3	-3	10^{25}	10^{25}	P
3	olivine	+2	-2	10^{25}	10^{25}	S(PB)
4	olivine	+3	-3	10^{25}	10^{25}	S(PB)
5	pyrolite	+2	-2	10^{25}	amb[*4]	S(SM)/A(CP)
6	pyrolite	+3	-3	10^{25}	amb	S(PB)/A(CP)
7	pyrolite	+2	-2	10^{23}	amb	S(SM)/A(SM)
8	pyrolite	+3	-3	10^{22}	10^{22}	S(PB)/A(CP)
9	olivine	+3	-3	10^{22}	10^{22}	S(PB)/A(CP)
10	pyrolite	+2	-2	GR[*5]	GR	P
11	pyrolite	+3	-3	GR	GR	S(SM)/A(CP)

*1: transition zone, *2: lower mantle

*3: Slab type

P: penetration without stagnation, S(PB): "phase-buoyancy" stagnation S(SM): "shape-memory" stagnation,

A(CP): "cold-plume" avalanche, A(SM): "shape-memory" avalanche

*4: ambient mantle viscosity defined by Eqs. (1) and (2), *5: grain-size reduction expressed by Eqs. (3) to (5)